The Galactic Chemical Evolution of Carbon: Implications for Stellar Nucleosynthesis

Daniel A. Boyea,[1★] James W. Johnson,[1] Third Author[2,3] and Others[1,3]
[1]Department of Astronomy, the Ohio State University, 191 W. Woodruff, Columbus, OH 43210, USA

Accepted XXX. Received YYY; in original form ZZZ

ABSTRACT

C is an important element across astronomy; however, its origin remains poorly understood. We aim to constrain the stellar yields of C through multi-zone Galactic chemical evolution models by comparing predictions with APOGEE subgiants abundances. We find that [C/Mg]-[Mg/Fe] is an emirical estimate of the delayed C sources, enabling us to estimate that AGB stars and CCSNe produce about 20% and 80% of C, respectively. The [C/Mg]-[Mg/H] trend instead represents the equilibrium abundances of C and Mg. We use the [C/Mg]-[Mg/H] trend to estimate the CCSNe C/Mg yield, determining that $y_{\rm C}^{\rm cc}/y_{\rm Mg}^{\rm cc} = EQUATION$ when including AGB C. Our models are relatively independent of uniform scaling of yields and outflows, and alternate star formation histories. However, the stars which contribute to AGB C production and the SNe Ia delay time distribution of Fe contribute uncertainties to our conclusions. While reliable gas-phase and low-metallicity measurments of C are challenging, we find that our model and a single-zone model with our recommended yields replicate the broad trends of [C/Mg]-[Mg/H] across different environments and metallicities.

1 INTRODUCTION

Carbon is a distinctive and well-studied element in astronomy. Formed in the cores of stars during He fusion, C is the lightest directly synthesized element after He, one of the only light elements formed in low-mass stars, and one the most abundant metals (e.g. Johnson 2019; Karakas & Lattanzio 2014).[1] C structurally changes the environments it pollutes – regulating stellar evolution, facilitating the formation of stars and planets, and forming the basis of earthly life. As such, understanding the origin of C has wide ranging implications. While we know both lower-intermediate-mass and high-mass stars produce C, the relative importance of each process is still unknown.

We know, from observations of MW stars and (extragalactic) gas, that C/O traces a banana shape in O/H (see Fig. 10 and section 5.5). At the very lowest metallicities, where $[{\rm O/H}] \lesssim -2$,[2] observations suggest that C/O declines with metallicity. From $-2 \lesssim [{\rm O/H}] \lesssim -1$, C/O is roughtly constant with metallicities. And, at higher metallicities $-1 \lesssim [{\rm O/H}]$, C/O increases with increasing metallicity. As our primary observational constraint, we use a sample of subgiant stars from the APOGEE (Majewski et al. 2017) selected by the criteria in Roberts et al. (2023, in prep). According to stellar evolution theory and observations, subgiants most accurately represent their birth composition (Gilroy 1989; Korn et al. 2007; Lind et al. 2008; Souto et al. 2018, 2019). Fig. 1 shows the subgiant sample plotted in [C/Mg]-[Mg/H] and [C/Mg]-[Mg/Fe]. [C/Mg] increases with metallicity, and [C/Mg] decreases with [Mg/Fe] at fixed [Mg/H]. Using the subgiant abundance trends, we will develop a model of the enrichment sources and evolution of C.

Galactic chemical evolution (GCE) is a powerful tool, capable of uncovering the origins of the elements. Each enrichment process has characteristic chemical signatures and timescales, enabling us to reconstruct chemical histories. Many previous works have used GCE in attemt to understand C abundances, whether through using theoretical stellar models (Dearborn et al. 1978; Prantzos et al. 2018; Chiappini et al. 2003) or understanding observation (Tinsley 1979; Henry et al. 2000; Bensby & Feltzing 2006; Rybizki et al. 2017; Berg et al. 2019; Kobayashi et al. 2020; See also review in Romano 2022). Every study agrees that C is produced by a combination of high-mass and lower-intermediate mass stars, different studies disagree on which process is dominant. For example CITES conclude high-mass stars dominate wherease CITES conclude lower-intermediate mass stars contribute the majority of C. C is also generally understood to have strong metallicity dependent CCSNe enrichment.

One of the primary uncertainties of GCE models are nucleosynthetic yields. Yield predictions – the amounts of each chemical element stars produce – are shaped by poorly understood processes, including mass loss, nuclear reaction rates, rotational mixing, convection, and explodability (Romano et al. 2010; Karakas & Lattanzio 2014; Ventura et al. 2013; Limongi & Chieffi 2018; Griffith et al. 2021). To better understand where C comes from and how it evolves, our aim is to combine APOGEE observations and multi-zone models to develop observationally-consistant yields. Johnson et al. (2023) examined similar GCE models of N (which is closely related to C), finding that trends in N and O are explained by the metallicity dependence of N/O yields. Johnson et al. (2023) determine that AGB N abundances roughly depend linearly on metallicity (i.e. $y_{\rm N}/y_{\rm O} \propto Z$). Here, we extend their models to C, deriving similar constraints on C/Mg yields. We assess which yield prescriptions reproduce Galactic abundance trends while investigating the impact of GCE model assumptions, such as the star formation history (SFH) and outflow mass loading.

[1] By metallicity, we mean the (mass) fraction of any element which is not H or He, denoted by Z. For the sun, we take $Z_\odot = 0.014$.

[2] In this paper, we use the standard notation for chemical abundances. $[A/B] = \log_{10}(A/B) - \log_{10}(A_\odot/B_\odot)$, i.e. $[A/B]$ is the logarithm of the ratio between A and B, scaled such that $[A/B] = 0$ for the sun. Solar abundances are as measured in Asplund et al. (2009).

2 DATA SELECTION

Subgiants provide the ideal observational constraint to our model. When a star enters the Red Giant Branch (RGB), material from the CNO-processed core is mixed with the envelope in first dredge up, enhancing N and depleting C (Iben 1967; Vincenzo et al. 2021; Karakas & Lattanzio 2014). RGB stars thus require model-dependent corrections to recover surface abundances (e.g. Vincenzo et al. 2021). On the other hand, gravitational settling can affect main sequence stellar abundances (e.g. Souto et al. 2019). Subgiants have well-mixed envelopes, so gravitational settling is not as significant, and subgiants have not yet experienced first dredge up. We use a sample of APOGEE DR17 stars (Majewski et al. 2017) as selected in Roberts et al. (2023, in prep.). Chemical abundances are determined from the APOGEE Stellar Parameter and Chemical Abundance Pipeline (ASPCAP) (García Pérez et al. 2016).

Fig. 2 shows a plot of all APOGEE stars and the Roberts et al. (2023, in prep.)polygon selection criteria. Roberts et al. (2023, in prep.) select a region of stars based on surface gravity $\log g$, and effective surface temperature, $T_{\rm eff}$.

$$\begin{cases} \log g \geq 3.5 \\ \log g \leq 0.004\,T_{\rm eff} - 15.7 \\ \log g \leq 0.000706\,T_{\rm eff} + 0.36 \\ \log g \leq -0.0015\,T_{\rm eff} + 12.05 \\ \log g \geq 0.0012\,T_{\rm eff} - 2.8. \end{cases} \tag{1}$$

Additionally, we exclude stars in APOGEE marked by any of the following flags.

```
APOGEE_MIRCLUSTER_STAR
APOGEE_EMISSION_STAR
APOGEE_EMBEDDEDCLUSTER_STAR
young cluster (IN-SYNC)
APOGEE2_W345
EB planet
```

Our final sample contains ~12,000 subgiants.

When plotting the data and models, we bin by groups of 500 (or 150) stars in [Mg/H] ([Mg/Fe]). When plotting [C/Mg]-[Mg/H], we select only the low-α sequence. For [C/Mg]-[Mg/Fe], we instead select stars with $-0.15 \leq$ [Mg/H] ≤ -0.05. When plotting [C/Mg]-[Mg/H], we isolate the low- and high-α sequences with the cut

$$\begin{cases} [\mathrm{Mg/Fe}] > 0.12 - 0.13\,[\mathrm{Fe/H}], & [\mathrm{Fe/H}] < 0 \\ [\mathrm{Mg/Fe}] > 0.12, & [\mathrm{Fe/H}] > 0. \end{cases} \tag{2}$$

The low-α sequence is better reproduced by this model, so we use this cut of the subgiants to compare the models against except for comparing [C/Mg]-[Mg/Fe].

3 NUCLEOSYNTHESIS

Table 1 contains our fiducial yields. For O, N, Mg, and Fe, we adapt the yield choices of Johnson et al. (2021, 2023). Following Johnson et al. (2021, 2023), we take the SNe Ia delay time distribution to be a $t^{-1.1}$ power-law with a minimum delay time of 140 Myr, as suggested by the observations of Maoz et al. (2012).

3.1 Asymptotic Giant Branch Stars

In this work, we explore four different sets of AGB star yield tables from literature, providing necessary well-sampled grids in mass and metallicity. We refer to the yields from the following studies as the following,

`C11`: Cristallo et al. (2011, 2015)
`K10`: Karakas (2010)
`V13`: Ventura et al. (2013, 2014, 2018, 2020)
`K16`: Karakas & Lugaro (2016); Karakas et al. (2018)

Table 2 contains the masses and metallicities used in each model.

Fig. 3 compares the stellar AGB C yields for these four models. We define the stellar AGB yield to be the fraction of the stars initial mass M which is newly synthesized into C. If $\Delta Z_{\rm C}$ represents the change in the mass fraction of C abundance, then

$$Y_{\rm C}^{\rm agb} = \Delta Z_{\rm C} \frac{M_{\rm ejected}}{M}. \tag{3}$$

Note that yields may be negative if the material returned to the interstellar medium has a lower abundance $Z_{\rm C}$ than the material the star was formed from. Most models agree on the qualitative shape of the net fractional AGB C yield. Stellar yields peak between masses of about 2–4 $\mathrm{M}_\odot$and decline as stars become more or less massive. As metallicity increases, the total AGB C yield decreases. The mass of peak C yields also increases slightly with metallicity.

The left panel of Fig. 4 shows IMF-averaged C yields for each AGB model as a function of metallicity. An IMF-averaged yield adds together the yields of stars of each mass, weighted by the fraction of stars of each mass (the IMF).

$$y_{\rm C}^{\rm agb}(Z,t) = \frac{\int_{M_{\rm to}(t)}^{8\,\mathrm{M}_\odot} Y_{\rm X}(M,Z)\frac{dN}{dM}\ M\ dM}{\int_{0.08\mathrm{M}_\odot}^{100\mathrm{M}_\odot} \frac{dN}{dM}\ M\ dM} \tag{4}$$

where dN/dM is the IMF and $M_{\rm to}(t)$ is the mass of stars with lifetime t. The AGB models mostly differ in their yield normalization and metallicity dependence. All yield models span a range of ~2 for a given metallicity. For example, all four models predict $y_{\rm C}^{\rm agb}(Z_\odot)$ to be between 0.004 and 0.008 at solar metallicity. The models also differ slightly in the strength of metallicity dependence, with about a factor of 3 discrepency (see Table 2).

Fig. 4, on the right, shows the total production of C by AGB stars in a SSP at an age t, i.e. $Y_{\rm C}(Z_\odot, t)$. As the mass range $2\,\mathrm{M}_\odot \lesssim M \lesssim 4\,\mathrm{M}_\odot$ is most important for C production, about half of C production occurs before ~1 Gyr, similar to SNe Ia Fe. `K10` and `K16` weight C production more heavily towards high-mass AGB stars resulting in a faster enrichment delay time, whereas the `C11` and `V13` models predict a slightly longer timescale of ~1 Gyr. In any case, little to no C is produced more than 2 Gyr after a star formation event. Fe production, in contrast, continues steadily for 10 Gyr.

Table 1. Yields for the fiducial model (in units of SSP birth mass). See section 3.1 for the definition of `C11`.

Element	$y^{\rm cc}$	$Y^{\rm agb}$	$y^{\rm ia}$
C	Eq. 11	2.4×`C11`	0
O	0.015	0	0
Mg	0.00185	0	0
Fe	0.0012	0	0.00214
N	0.00072	$0.0009M\left(\frac{Z}{Z_\odot}\right)$	0

[2] In our model, the mass-lifetime relation is $\log \tau_M = 1.02 - 3.57 \log M + 0.90\,(\log M)^2$, where τ_M is in Gyr, from Larson 1974. We use $t_{\rm end} = 10$ Gyr for total yields when t is not used.

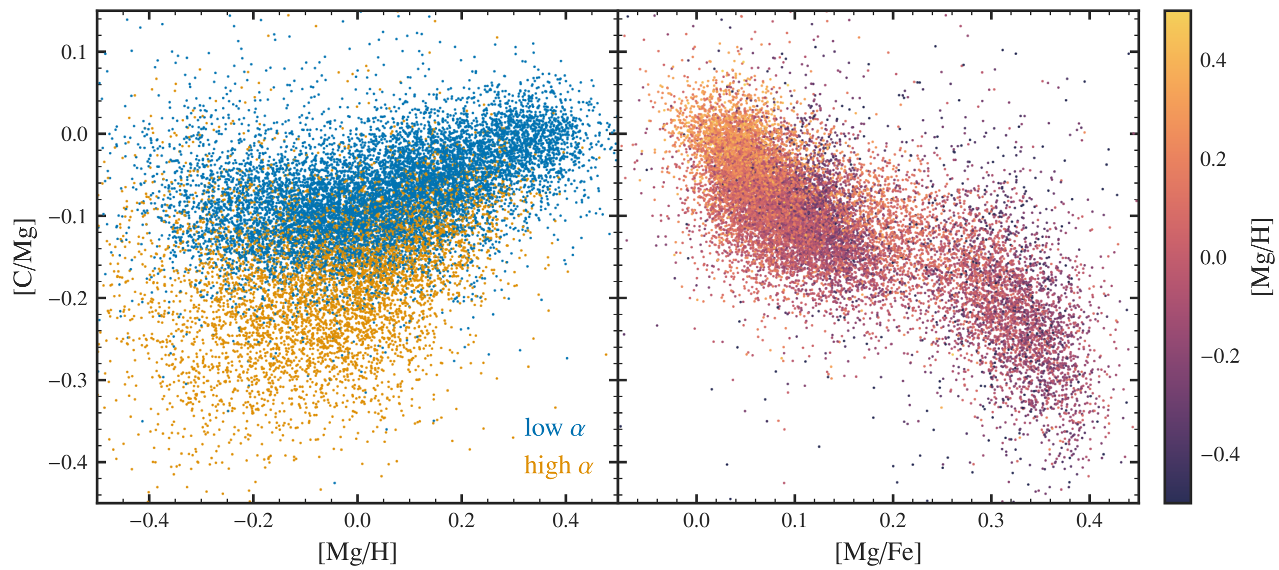

Figure 1. The [C/Mg] ratio against [Mg/H] (top) and [Mg/Fe] (bottom) for the Roberts et al. (2023, in prep.) sample of APOGEE subgiants. On the top, we plot high and low-α stars in blue and orange, using the separation defined in Equation 2 (the high and low-α stars are named for their high or low α-element to Fe ratios, or in this case, Mg/Fe). On the bottom, we colour-code stars according to their [Mg/H] abundance.

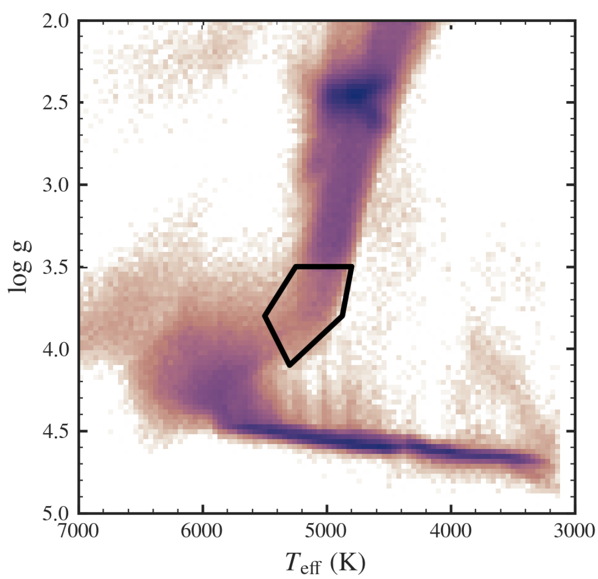

Figure 2. A Kiel diagram of APOGEE stars. Following Roberts et al. (2023, in prep.), we select subgiants in the black pentagon (see Equation 1). These stars have not yet experienced first dredge-up, so their photospheric C and N abundances should reflect their birth mixture.

In an AGB star, two competing processes determine the outcome of C production: *third dredge up* and *hot bottom burning*. Third dredge up accompanies thermal pulses in AGB stars, where material from the CO core is mixed with the envelope, increasing surface C abundances (Karakas & Lattanzio 2014). The C yields of the star are increased as this C-enhanced envelope is released to the interstellar medium. Hot bottom burning is the activation of the CNO cycle[3] at the bottom of the convective envelope when $T \gtrsim 50\,\mathrm{MK}$. Because the ^{14}N proton capture is the slowest component of the CNO cycle, the CNO cycle converts nearly all ^{12}C into ^{14}N (Adelberger et al. 2011).

Hot bottom burning and third dredge-up result in mass and metallicity dependent C yields. Stars less than $\sim 2\,\mathrm{M}_\odot$ do not experience third dredge-up. As a result, these stars C abundances are only affected by first dredge-up, resulting in little change to C yields or slight destruction of C. Above $\sim 2\,\mathrm{M}_\odot$, third dredge up becomes important, enriching the outer layers with C. AGB stars between 2 and 5 $\mathrm{M}_\odot$ are the most abundant producers of C. In AGB stars more massive than $\sim 5\,\mathrm{M}_\odot$, both hot bottom burning and third dredge up occur; however, hot bottom burning is much more efficient, resulting in significant ^{12}C destruction. Metal poor stars dredge up more material due to the decreased power of the CNO cycle, resulting in increasing carbon yields with decreasing metalicity (Ventura et al. 2013).

For our models to match observations, we find that need to uniformly amplify these yield tables.

$$y_{\rm C}^{\rm agb} \rightarrow \alpha_{\rm agb}\, y_{\rm C}^{\rm agb}. \tag{5}$$

We use `C11` table, with $\alpha_{\rm agb} = 2.4$, as the fiducial AGB yield. Variations in models are due to different treatments of reaction rates, convection, and mass-loss. Table 2 contains the stellar masses and metallicites each yield set contains, the approximate solar C yield $y_{\rm C}^{\rm agb}(Z_\odot)$, the metallicity dependence at solar $\zeta^{\rm agb} = dy_{\rm C}^{\rm agb}/dZ$, and the required factor α to reach 20% AGB C production.

3.2 Core Collapse Supernovae

Massive stars form ^{12}C in their cores through the triple–α process. However, only C ejected through supernovae and stellar winds contributes to the yield. While there are many stellar models providing

[3] The CNO cycle is a series of proton-capture reactions with CNO elements resulting in energy generation and the creation of an α particle. $^{12}\mathrm{C}(\mathrm{p},\gamma)^{13}\mathrm{N}(\beta^+,\nu_e)^{13}\mathrm{C}(\mathrm{p},\gamma)^{14}\mathrm{N}(\mathrm{p},\gamma)^{15}\mathrm{O}(\beta^+,\nu_e)^{15}\mathrm{N}(\mathrm{p},\alpha)^{12}\mathrm{C}$. There are other less important minor branches of the CNO cycle (Adelberger et al. 2011).

Table 2. For each AGB yield set, the IMF-averaged AGB C yield at solar metallicity $y^{\rm agb}_{\rm C,0}$ and the multiplicative factor reaches an AGB contribution of 20% $\alpha_{\rm agb,20}$.

AGB table	$y^{\rm agb}_{\rm C}(Z_\odot)$	$\zeta^{\rm agb}(Z_\odot)$	$\alpha^{\rm agb}_{20}$	masses ($M_\odot$)	metallicites
C11	0.00042	-0.0175	2.4	1.3, 1.5, 2, 2.5, 3, 4, 5, 6	0.0001, 0.0003, 0.001, 0.002, 0.003, 0.006, 0.008, 0.01, 0.014, 0.02
K10	0.00064	-0.059	1.6	1, 1.25, 1.5, 1.75, 1.9, 2.25, 2.5, 3, 3.5, 4, 4.5, 5, 5.5, 6	0.0001, 0.004, 0.008, 0.02
V13	0.00022	-0.021	4.5	1.5, 2, 2.5, 3, 3.5, 4, 4.5, 5, 6, 6.5, 7	0.0003, 0.001, 0.002, 0.004, 0.008, 0.014, 0.04
K16	0.0005	-0.029	2.0	1, 1.25, 1.5, 1.75, 2.25, 2.5, 2.75, 3, 3.25, 3.5, 3.75, 4, 4.5, 5, 5.5, 6, 7	0.0003, 0.001, 0.002, 0.004, 0.008, 0.014, 0.04

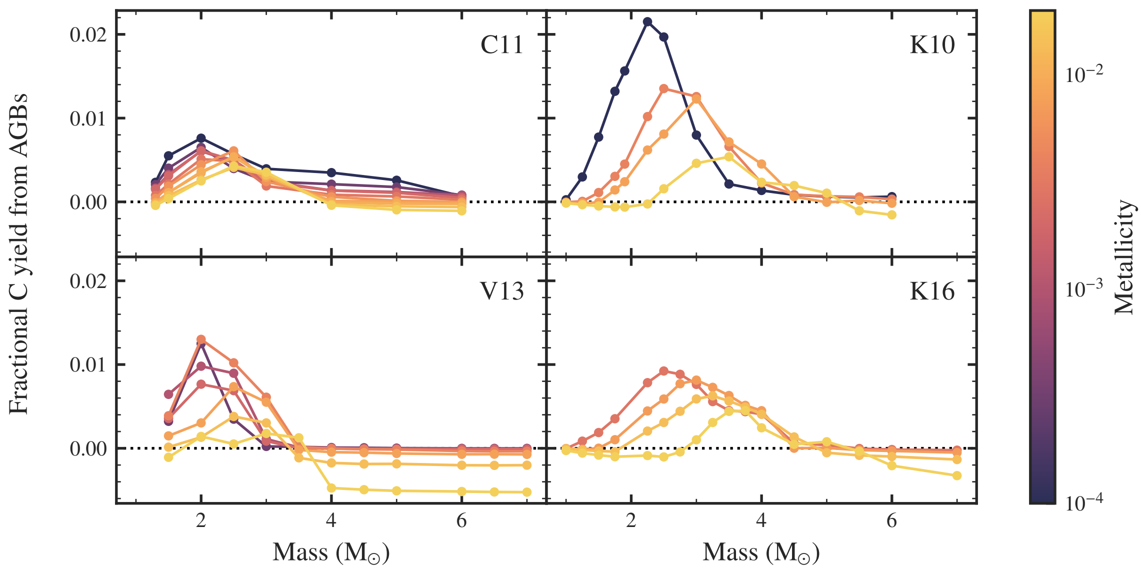

Figure 3. The net fractional AGB C yield plotted as a function of initial stellar mass M and colour-coded according to metallicity. The black dashed line shows $Y = 0$ for reference. Each panel represents yields from one of four AGB models: C11, K10, V13, K16, and our analytic model (see sections 3.1)

predictions of CCSNe yields, the results of these models are highly uncertain due to the complexity of stellar modeling.

Fig. 5 plots calculations of the IMF-integrated yields. For CCSNe

$$y^{\rm cc}_{\rm C}(Z) = \frac{\int_{8\,{\rm M}_\odot}^{100\,{\rm M}_\odot} Y_{\rm X}(M,Z)\frac{dN}{dM}\,M\,dM}{\int_{0.08{\rm M}_\odot}^{100{\rm M}_\odot}\frac{dN}{dM}\,M\,dM} \qquad (6)$$

where dN/dM is the IMF and $M_{\rm to}(t)$ is the mass of stars with lifetime t.CCSNe models predict a wide range of C yields, spanning almost a factor of ten. Both the Nomoto et al. (2013) and Limongi & Chieffi (2018) models show positive metallicity dependence. As metallicity increases, stars lose more of their mass to winds. In particular, C enriched envelop material is lost through winds before synthesized into heavier elements, so C yields can be strongly metallicity dependent (VERIFY). Fig. 5 shows the C11 AGB model for comparison on the left. Especially at $Z \approx Z_\odot$, most CCSNe models dominate AGB C production. Later, we will also show empirically this is the case. The right of Fig. 5 shows the CCSNe [C/Mg] ratio for the different models, defined by

$$[{\rm C/Mg}]^{\rm CC} = \log_{10}\left(\frac{y^{\rm cc}_{\rm C}}{y^{\rm cc}_{\rm Mg}}\right) - \log_{10}\left(\frac{Z_{\rm C,\odot}}{Z_{\rm Mg,\odot}}\right). \qquad (7)$$

If only CCSNe produced C, then $[{\rm C/Mg}]^{\rm CC}$ describes the equilibrium abundance of [C/Mg]. Different CCSNe models also span a large range in [C/Mg].

Rotation, binarity, and explodability introduce substantial uncertainties in CCSNe predictions. The Limongi & Chieffi (2018) models include rotation, showing that variations in the rotational velocity of the star can dramatically increase the magnitude and metallicity dependence of $y^{\rm cc}_{\rm C}$. Rotation induces more mixing allowing the CO core to grow larger and contributes to wind losses. As we will later show, CCSNe C production needs to be strongly metallicity-dependent at $Z/Z_\odot \approx 1$, which is consistent with the Limongi & Chieffi (2018) rapidly rotating models. Assumptions about the explodability landscape affect C and Mg production. As fewer high-mass stars explode, both C and Mg yields decrease, but Mg yields decrease more as more C is lost to winds, so [C/Mg] increases with decreasing explodability. Finally, stripped binaries produce about twice as much C as single massive stars and other effects of binary evolution are unstudied (Farmer et al. 2021).

CCSNe do not satisfactorily explain C, O, and Mg abundances. Most models here overproduce C relative to Mg. This could be related to overproduction of O relative to Mg, a known problem of CCSNe models. There is substantial variation in predicted Mg yields but most models predict flat trends. However, the variation is significant and

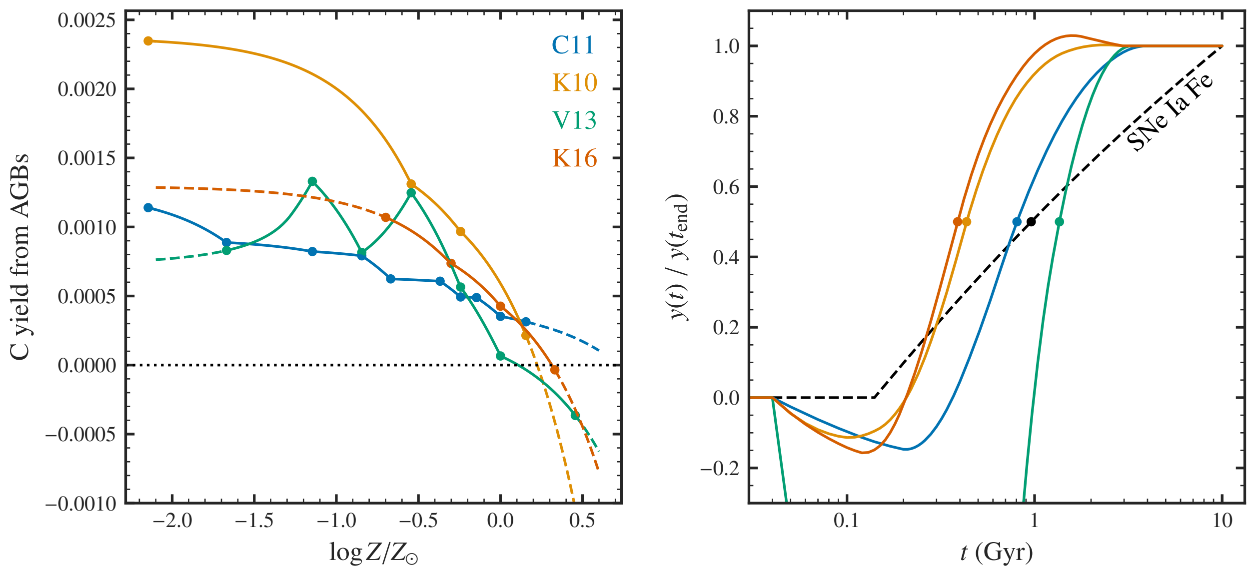

Figure 4. C yields from AGB stars as a function of SSP age, as a fraction of the C yield at $t_{\rm end} = 10\,$Gyr. **Left** The (IMF-weighted) AGB C yield $y_{\rm C}^{\rm agb}$ as a function of metallicity for each of the AGB yield models. ($y_{\rm C}^{\rm agb}$ is the net mass of C produced by AGB stars per unit mass of star formation, after 10 Gyr and assuming a Kroupa 2001 IMF.) **Right** Our four considered AGB yield models at solar metallicity (`C11`, `K10`, `V13`, `K16`. The dashed red line shows the delay time distribution of type Ia supernovae ($\propto t^{-1.1}$) for comparison, and the minimum of V13 is $y(t)/y(t_{\rm end} = -3.3$.

our adopted $y_{\rm Mg}^{\rm cc}$ yield is much higher than most models, but O and Mg yields of CCSNe models do not fully match observations. CCSNe models underpredict [Mg/O], and the reason why is unknown (see e.g. Griffith et al. 2021). Here, we assume [O/Mg] = 0, which nevertheless consistent with APOGEE observations (Weinberg et al. 2019, 2022). As we focus on constraining relative yields, we neglect O and Mg yield variations in the main text, leaving them constant and metallicity-independent. We also choose to parameterize C yields.

3.3 Equilibrium Abundances

Galaxies, when moderated by metal-poor gas accretion and feedback-driven outflows, reach a chemical equilibrium. The production of new metals is balanced by losses to new stars and outflows (Larson 1972; Dalcanton 2007; Finlator & Davé 2008; Peeples & Shankar 2011; Lilly et al. 2013). Here, we assume a simple *one-zone* chemical evolution model (e.g. Tinsley 1980; Pagel 2009; Matteucci 2021). While our galaxy is likely not in perfect equilibrium or described by a single, homogeneous chemical envirnoment, the equilibrium approximation is nevertheless useful in understanding yields and metallicity dependence of solar neighborhood stars (e.g. Johnson et al. 2022, 2023; Weinberg et al. 2017).

Johnson et al. (2023) show that trends in N and O abundance ratios are set by the yield ratio and their metallicity dependences. Here, we find a similar conclusion for C and Mg (see section xxx in Johnson et al. 2021), where equilibrium C/Mg is given by

$$\frac{Z_{\rm C}^{\rm eq}}{Z_{\rm Mg}^{\rm eq}} = \frac{y_{\rm C}^{\rm cc} + y_{\rm C}^{\rm agb}}{y_{\rm Mg}}. \tag{8}$$

In Fig. 6, we show the inferred total C yields, based on this equation, and our best fitting linear model. From a linear regression, we suggest that

$$\frac{y_{\rm C}(Z)}{y_{\rm O}} \approx \frac{1}{3} + 4\left(Z - Z_\odot\right) \tag{9a}$$

$$\frac{y_{\rm C}(Z)}{y_{\rm Mg}} \approx 2.7 + 32\left(Z - Z_\odot\right). \tag{9b}$$

These yield ratios results in an equilibrium abundance [C/α] = −0.09 at solar metallicity, which is consistent with the subgiant sample and is within ~20% of the solar C/Mg mixture from Asplund et al. (2009).

Both observational and theoretical uncertainties limit the accuracy of our relative yield predictions. Additionally, the derived yields will be systematically biased if the galaxy is out of equilibrium, for example, due to a recent starburst (Mor et al. 2019; Isern 2019).

With the total C yield of Eq. 9 and given an AGB C yield, we can derive an observationally-consistant CCSNe C yield.

$$y_{\rm C}^{\rm cc}(Z_\odot) = y_{\rm C}(Z_\odot) - y_{\rm C}^{\rm agb}(Z_\odot) \tag{10a}$$

$$\zeta^{\rm cc} \equiv \frac{dy_{\rm C}^{\rm cc}(Z_\odot)}{dZ} = \frac{dy_{\rm C}(Z_\odot)}{dZ} - \frac{dy_{\rm C}^{\rm agb}(Z_\odot)}{dZ} \tag{10b}$$

This method reduces the number of free parameters of the model and enables all models to match [C/Mg]-[Mg/H] trends in APOGEE subgiants when considering AGB yields with different metallicity dependences and normalizations. We use values of $y_{\rm C}^{\rm agb}$ and $\zeta^{\rm agb}$ as presented in Table 2. For example, in our fiducial model, $y_{\rm C}^{\rm cc} = 0.004 + 0.102(Z - Z_\odot)$. Our full CCSNe C yield model adds a low-metallicity enhancement term, which is insignificant at solar metallicities (e.g. thin disk stars) but enables models in section 5.5 to match low-metallicity environments. We parameterize low-metallicity enrichment with y_l and Z_l, the yield and transition metallicity for enhanced low-metallicity yields. All-together,

$$y_{\rm C}^{\rm cc} = y_{\rm C,0}^{\rm cc} + \zeta^{\rm cc}\left(Z - Z_\odot\right) + \frac{2\,y_l}{1 + Z/Z_l}. \tag{11}$$

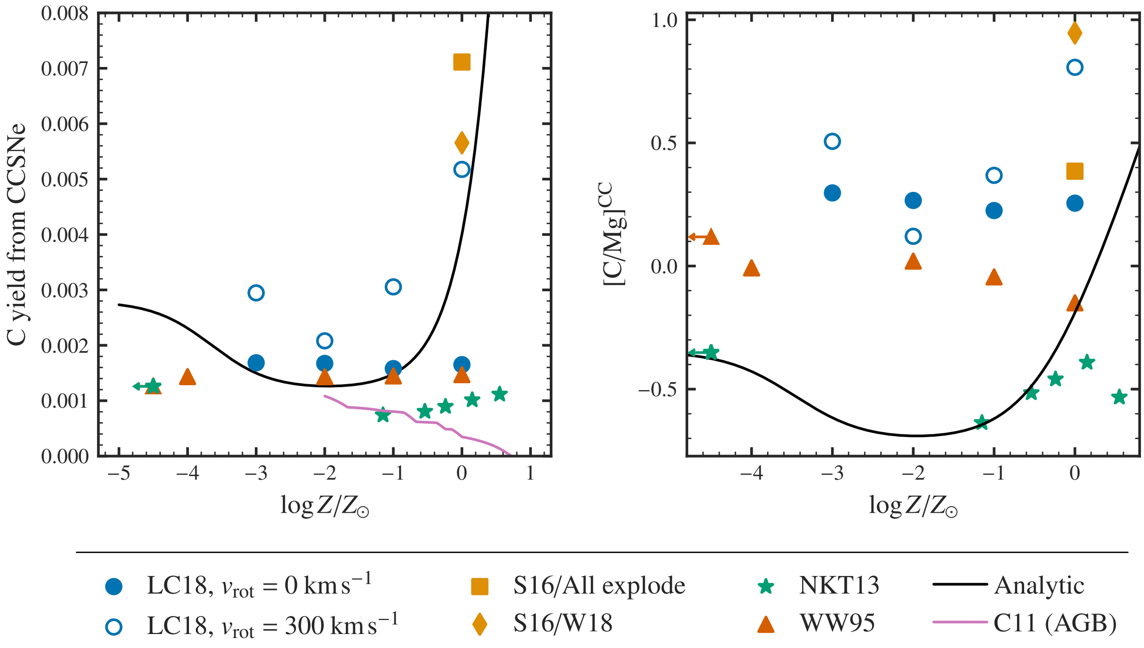

Figure 5. C yields from high-mass stars. **Left** The IMF-weighted CCSNe yield of C as a function of metallicity. **Right** The CCSNe [C/Mg] abundance ratio, defined in Eq. 7. The black line is the derived C yield from section 3.3 and Eq. 11. Yields are shown for tables from Woosley & Weaver (1995, red triangles), Sukhbold et al. (2016, orange squares and diamonds), Nomoto et al. (2013, green stars), and Limongi & Chieffi (2018, blue circles). Sukhbold et al. (2016) report yields for different black hole landscapes, while Limongi & Chieffi (2018) provide yields at different rotational velocities. In the top panel, the pink line denotes $y_{\rm C}^{\rm agb}$ from C11 for comparison. All models include wind yields.

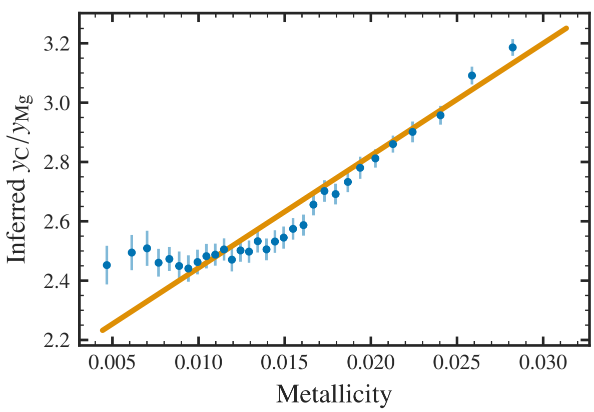

Figure 6. Inferred total C yields as a function of metallicity. We assume chemical equilibrium (orange curve, see discussion in section 3.3). Blue points are the median value of $y_{\rm C}^{\rm cc}$ for each (number) bin in [Mg/H] with uncertainties based on the 16–84 percentile range.

4 THE MULTI-ZONE MODEL

Our models extends the Johnson et al. (2021, hereafter J21) Milky Way model, run with the publicly available Versatile Integrator for Chemical Evolution (VICE).[4] This model is described extensively in J21 and concisely summarized in Johnson et al. (2023). Here, we provide a brief overview of the relevant model components. Classical, *one-zone* models of chemical evolution assume instantaneous mixing of metals in the star-forming interstellar medium (e.g. Matteucci 2021). This simple framework is a poor approximation of the Milky Way. The Galaxy evolves *inside-out* – where star formation is higher towards the center and in the early universe (Bird et al. 2013). Additionally, stars can migrate several kpc over their lifetimes, mixing different chemical environments across the galaxy (Bird et al. 2012; Sellwood & Binney 2002). Multi-zone models account for stellar migration and changing environments by including multiple zones with different chemical conditions which stars can move between.

Star formation is set seperately for each zone. The Galaxy is divided into 200 rings, each 100 pc wide representing a single zone. Each ring (or zone) has a separate stellar population and gas supply. We initially assume an inside-out SFH, where the star formation surface density $\Sigma_\star$ is given by

$$\dot{\Sigma}_\star \propto \left(1 - e^{-t/\tau_{\rm rise}}\right) e^{-t/\tau_{\rm sfh}}. \tag{12}$$

$\tau_{\rm rise} = 2$ Gyr describes when the star formation rate reaches a maximum, and $\tau_{\rm sfh}$ describes the decay timescale of star formation as a function of radius R. J21 derives $\tau_{\rm sfh}(R)$ through analysis of four integral field spectroscopy surveys in Sánchez (2020). At each R, the SFH is normalized to match the stellar surface density gradient (Bland-Hawthorn & Gerhard 2016) and the total stellar mass reaches $5.17 \times 10^{10}\,{\rm M}_\odot$ (Licquia & Newman 2015). Star formation ends beyond a radius $R = 15.5$ kpc. The gas inflow is calculated to maintain the SFH for each radius and time, using an extension of a Kennicutt-Schmidt law (Kennicutt 1998),

$$\dot{\Sigma}_\star \propto \begin{cases} \Sigma_{\rm gas} & 2\times10^7 \le \Sigma_{\rm gas} \\ (\Sigma_{\rm gas})^{3.6} & 5\times10^6 \le \Sigma_{\rm gas} < 2\times10^7 \\ (\Sigma_{\rm gas})^{1.7} & \Sigma_{\rm gas} < 5\times10^6 \end{cases} \tag{13}$$

[4] VICE is available at https://github.com/giganano/VICE

where $\Sigma_{\rm gas}$ is measured in $\rm M_\odot\ kpc^{-2}$. The scaling of this relationship varies with time due to the redshift dependence of $\tau_\star$ in molecular gas observed by Tacconi et al. (2018). We assume a Kroupa (2001) IMF.

To account for radial migration, we use a Gaussian-based migration scheme. The $\Delta R \propto \sqrt{\rm time}$ dependence arises when migration proceeds as a consequence of the diffusion of angular momentum (Frankel et al. 2018, 2020). As such, at each time step, each star particle moves some change in radius, based on

$$\delta R \sim N(0, \sigma_R) \tag{14a}$$

$$\sigma_R = 1.27\,{\rm kpc}\left(\frac{dt}{1\,{\rm Gyr}}\right)^{0.5} \tag{14b}$$

where $N(\mu, \sigma)$ represents a draw from normal distribution. We do not account for radial gas flows. Not shown here, we also explore migration based on the h277 hydrodynamical simulation results (with simulation parameters as in Bird et al. 2021; see also Christensen et al. 2012; Zolotov et al. 2012; Loebman et al. 2012; Brooks & Zolotov 2014), which leaves our qualitative conclusions unchanged. The full impact of the details of a galaxy's dynamical history on its chemical evolution is still unknown.

As the strength of outflows controls the resulting α-element abundances, J21 create a metallicity gradient by defining

$$\eta(R) = r - 1 + \frac{y_\alpha^{\rm CC}}{Z_{\alpha,\odot}} 10^{(-0.08\,{\rm kpc}^{-1})(R-4\,{\rm kpc})+0.3}. \tag{15}$$

This choice of $\eta(R)$ results in a [α/H] gradient consistent with Milky Way observations (e.g. Hayden et al. 2014; Weinberg et al. 2019; Frinchaboy et al. 2013). Note that if we change our assumed $y_{\rm Mg}$, the values of η will change similarly to maintain the correct chemical trends.

To create a sample with similar characteristics of the subgiant observations, we sample 12,000 stars from the simulations such that the cumulative distribution function of stars in $R_{\rm gal}$ is the same for the subgiants and our comparison sample.

5 RESULTS

5.1 Evolution of Carbon Abundances

Here, we present the time evolution of our fiducial model. In the next sections, we will discuss the choice of parameters and agreement with observations. The fiducial model has the following qualitative characteristics of its C yields.

C is mostly (~80%) produced in CCSNe
CCSNe produce more C at higher metallicities
AGB stars produce less C at higher metallicities

The fiducial model uses the C11 AGB yield tables uniformly scaled by a factor of 2.4 (see section 3.1, and Table 1).

Fig. 7 shows time evolution tracks of the fiducial model for [C/Mg]-[Mg/H] and [C/Mg]-[Mg/Fe]. As discussed in section 3.3, [C/Mg]-[Mg/H] is set by the total C/Mg yields. [C/Mg]-[Mg/Fe] is instead useful in understanding delayed C production. As both Fe and C are delayed elements, [Mg/Fe] steadily decreases after a star formation event, unlike [Mg/H] which quickly reaches equilibrium. All plots showing [C/Mg]-[Mg/Fe] going forward are selected in metallicity such that $-0.15 \le [\rm Mg/H] \le -0.05$, so metallicity-dependent yields do not affect this plot. The [C/Mg]-[Mg/Fe]-diagram is, in essence, an emperical delay-time-distribution for a single stellar population of C, especially as we assume a $\propto t^{-1.1}$ delay-time-distribution for Fe. Comparing the left and right panels of Fig. 7 highlights the differences between [C/Mg]-[Mg/H] and [C/Mg]-[Mg/Fe]. While [C/Mg]-[Mg/H] quickly reaches its final equilibrium distribution (within ~5 Gyr), [C/Mg]-[Mg/Fe] continues to evolve in both [Mg/Fe] and [C/Mg] until the simulation ends.

C evolution proceeds as follows,

(i) CCSNe initially dominate production. As $y_{\rm C}^{\rm cc}$ has strong metallicity dependence, [C/Mg] increases with time.
(ii) AGB stars contribute delayed C, causing [C/Mg] to increase even faster with [Mg/H].
(iii) [C/Mg] plateaus as C also approaches equilibrium.
(iv) [C/Mg] may decrease due to declining SFH or slightly negative yields from ~1 $\rm M_\odot$ stars.

5.2 Yield Variations

CCSNe, which we assume make up the majority of C, set the overall C abundance trends. The top of Fig. 8 shows models with varying $y_{\rm C}^{\rm cc}$ metallicity dependence, $\zeta^{\rm cc}$. As the [C/Mg]-[Mg/H] trend is approximated by equilibrium trends, the models with higher $\zeta^{\rm cc}$ also have a steeper slope in [C/Mg]-[Mg/H]. However, [C/Mg]-[Mg/Fe] is minimally affected by changes to $\zeta^{\rm cc}$ since CCSNe occurs on much shorter timescales than SNe Ia and AGB enrichment. The only effects on [C/Mg]-[Mg/Fe], when considering the narrow metallicity slice, are because of either the slight change in equilibrium abundances, the imperfect evolution of the galaxy, or that the interstellar medium abundances are set by stars which were born at poorer metallicities. Hence, [C/Mg]-[Mg/H] tells us about the total C yield with metallicity, which [C/Mg]-[Mg/Fe] is independent of. If we know the AGB C yields, then with observed [C/Mg]-[Mg/Fe] abundance trends, we can infer the CCSNe C yields with metallicity.

To parameterize the AGB contribution to C production, we define $f_{\rm agb}$ to be the fraction of C which comes from AGB stars.

$$f_{\rm agb} \equiv \frac{y_{\rm C}^{\rm agb}(Z = Z_\odot)}{y_{\rm C}(Z = Z_\odot)}, \tag{16}$$

We can use the [C/Mg]-[Mg/Fe] diagram of APOGEE stars to estimate the delayed portion of C. When binned in metallicity, median [C/Mg] changes by about 0.2 dex across the range of [Mg/Fe] at solar metallicities. As high-α stars have little to no delayed SNe Ia Fe, these stars would also have little to no delayed AGB C. This means that AGB C stars make up about at most a fraction $f_{\rm agb} \approx 1 - 10^{-0.2} \approx 0.4$ of C production.

[C/Mg]-[Mg/Fe] is sensitive to the assumptions about delayed C from AGB stars. If no C comes from low-mass stars, then [C/Mg] would be independent of [Mg/Fe], only [Mg/H]. Instead, C shows strong trends in [C/Mg]-[Mg/Fe] independent of metallicity.

In the middle row of Fig. 8, we first show the four C yield models (K10, K16, C11, V13). For the most part, the AGB yield sets result in qualitatively similar predictions. V13, however, does not reproduce solar trends as the model predicts strong C production at slightly above solar metallicities, resulting in a decreasing [C/Mg] with [Fe/Mg]. As all AGB models predict some low-mass C destruction, each model does predict a downturn in [C/Mg] as [Fe/Mg] increases. A recent burst in star formation may hide this downturn (see section 5.3), but the C destruction is not supported directly by observations.

We also investigate adjustments to the AGB yield fraction $f_{\rm agb}$ The bottom of Fig. 8 shows three models with different AGB fractions while using C11 yields. The [C/Mg]-[Mg/Fe] relationship is set by

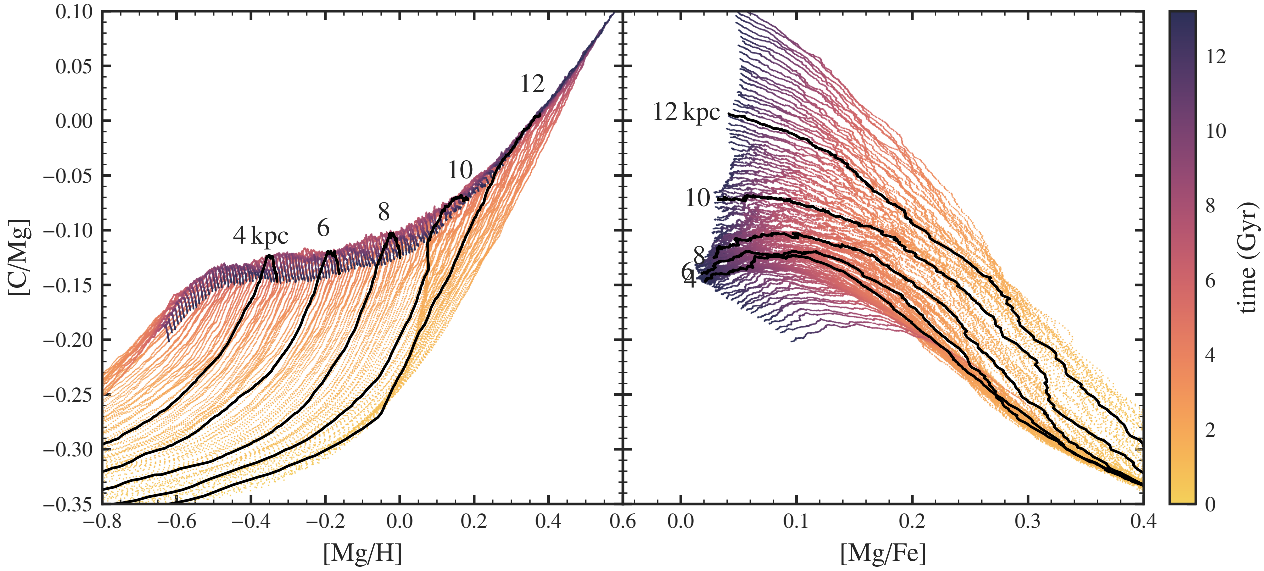

Figure 7. Time evolution of gas-phase C abundances in our fiducial model. Each line represents a zone at a different galactic radii. The lines are coloured-coded by time. The left shows [C/Mg]-[Mg/H] and the right [C/Mg]-[Mg/Fe].

$f_{\rm agb}$ because a specific amount of C must be released at a delayed time to match the SNe Ia production of Fe and increase [C/Mg] as [Mg/Fe] decreases to reproduce the data. Increased $f_{\rm agb}$ results in a decreased slope in [C/Mg]-[Mg/H], owing to the negative metallicity dependence of $y_{\rm C}^{\rm agb}$. So while [C/Mg]-[Mg/H] alone cannot differentiate models which vary $f_{\rm agb}$ and ζ correspondingly, [C/Mg]-[Mg/Fe] provides information on $f_{\rm agb}$. So, we can use [C/Mg]-[Mg/Fe] to estimate $f_{\rm agb} \approx 0.2$, and then choose ζ to match [C/Mg]-[Mg/H].

5.3 Star Formation History and Outflows

In this section, we consider two modifications of our fiducial SFH: *lateburst* and *earlyburst*. Our lateburst model adds a Gaussian factor to the inside-out SFH,

$$\dot{\Sigma}_{\rm lateburst} \propto \dot{\Sigma}_{\rm inside\text{-}out} \left(1 + A\, e^{-(t-\tau_{\rm burst})^2/2\sigma_{\rm burst}^2}\right) \tag{17}$$

where $A = 1.5$ represents the amplitude of the birth, $\tau_{\rm burst} = 10.8$ Gyr is the time where the burst is strongest, and $\sigma_{\rm burst} = 1$ Gyr is the width of the burst.

The middle row of Fig. 8 shows three models with our alternate SFH. Changes to the SFH leave [C/Mg]-[Mg/H] unchanged, but they do introduce slight variation in [C/Mg]-[Mg/Fe]. Models with higher AGB fractions are more sensitive to variations in the SFH. The late burst models result in [C/Mg] continuing to increase at low [Mg/Fe], but also introduce a dip not present in the data. Additionally, the early-burst reproduces the slight break between the low and high α sequences, but overshoots equilibrium more severely than the fiducial model. In general, any of these SFHs are consistent with this model.

5.4 Degeneracies

Our conclutions are limited by the many uncertainties in GCE modeling.

A known uncertainty is the overall scaling of outflows and yields. While Milky Way GCE models like ours incorperate significant mass-loading, others neglect mass-loading and instead use lower yields (e.g. Minchev et al. 2013, 2014; Spitoni et al. 2019, 2020, 2021). Our parameterization of η illustrates this (see Equation 15) – lowering y_α will additionaly lower our values of η. We consider a model where our adapted values of all yields are halved, in the bottom row of Fig. 8. This change does not affect our results.

An addition source of theoretical uncertainty in this result is that the SNe Ia yield and delay time distributions have their own uncertainties. Increasing both $y_{\rm Fe}^{\rm Ia}$ and $y_{\rm C}^{\rm agb}$ correspondingly leaves [C/Mg]-[Mg/Fe] mostly unchanged. We show a model where we increase SNe IaFe yields by 20% and increase $f_{\rm agb}$ to 0.3, leaving median trends unchanged.

Finally, the specific masses of AGB stars do affect the delay-time-distribution. If AGB are produced more by $\sim$1 M$_\odot$stars than upper-intermediate AGB stars, then the delay-time-distribution of AGB C is more extended. In this case, a On the other hand, upper-intermediate AGB stars with masses greater than 5 M$_\odot$have lifetimes less than about 100 Myr, which is only slightly longer than CCSNe. As such, changes to the amount of C from CCSNe and 5–8M$_\odot$AGB stars is nearly indestinguashible from median abundance trends alone.

5.5 Gas-Phase Abundances

As a final test of the model, we compare the model predictions against gas-phase measurements. Fig. 10 shows the fiducial model's gas-phase predictions compared to observations of the Milky Way and extragalactic HII regions, halo stars, and damped Lyman-alpha systems. While obervations in HII regions and Milky Way stars agree that C/O generally increases at near-solar metallicities, damped Lyman-alpha systems and metal poor stars imply that C/O may also increase again at very low metallicities.

Measurements of C abundances are challenging. In HII regions, C/O abundance ratios are measured with either recombination lines or collisional excitation lines. While broad consistancy of our model with gas-phase measurments is promising, the large measurment errors limit the evaluative power of HII regions. We additionally include Milky Way thick disk (high-α) and halo stars, which span a

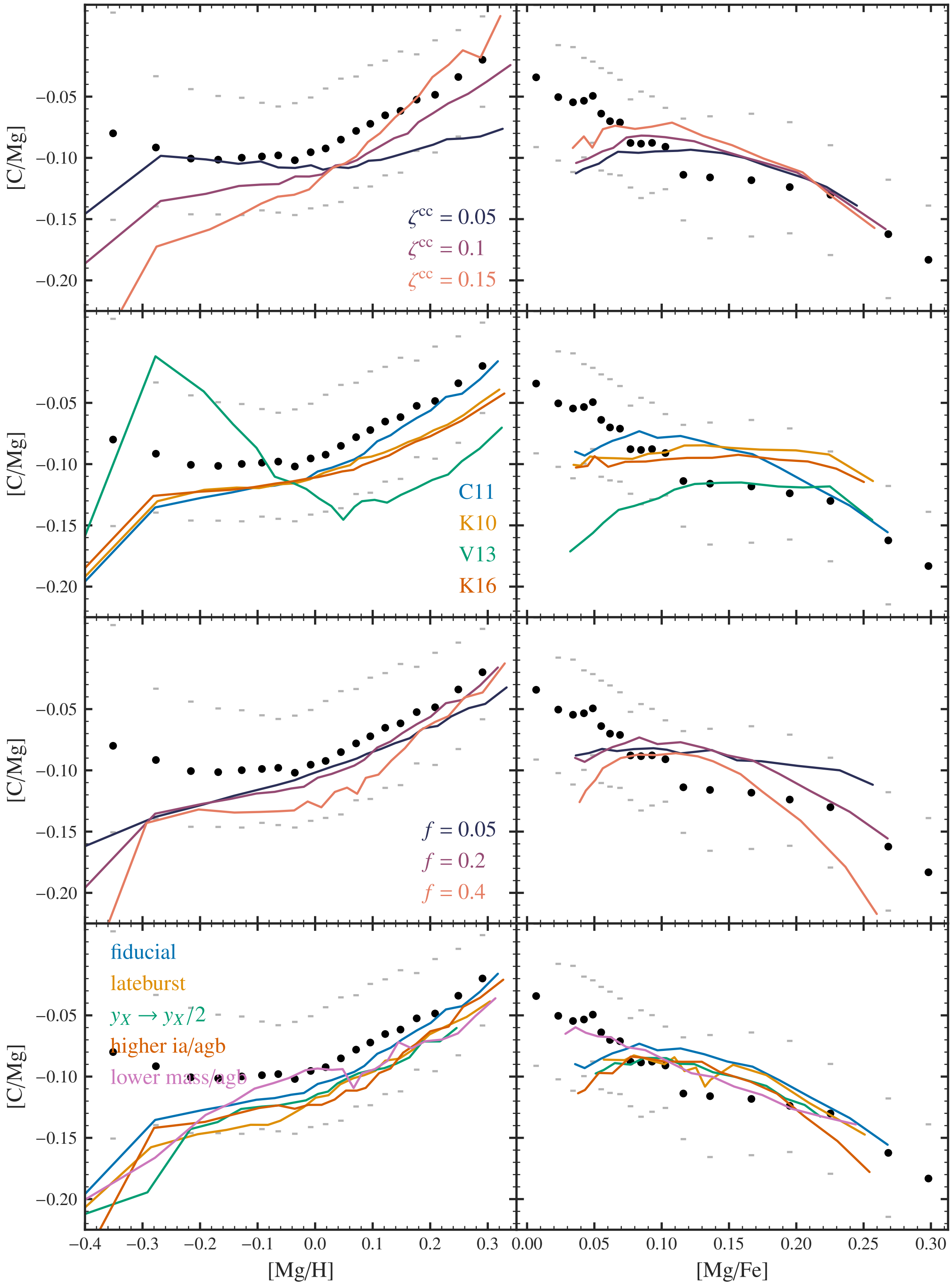

Figure 8. Stellar abundance trends in our model, assuming metallicity independent y_C^{cc}. Coloured lines represent the median [C/Mg] in bins of [Mg/H] (left) or [Mg/Fe] (right) for each model. Black points and grey dashes represent the median and standard deviations of [C/Mg] for each [Mg/H] bin in the Roberts et al. (2023, in prep.) sample. In the right panels, we show the trends only for stars where $-0.15 \leq$ [Mg/H] ≤ -0.05. **Top**: Models with different metallicity dependences for CCSNe C yiels. **Middle**: Our four different AGB models. **Bottom**: Different AGB fractinos of C.

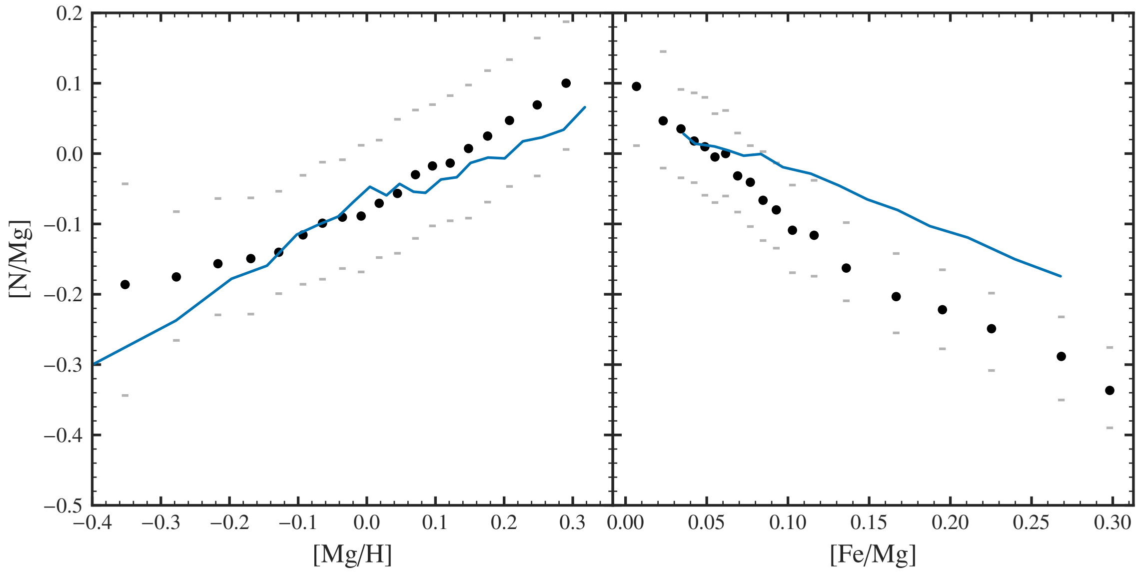

Figure 9. Similar to Fig. 8. The top panels show models with different mass-ranges contributing AGB C yields. The middle panels show different star formation histories (section 5.3) and yield normalizations. The bottom panels show [N/Mg] against [Mg/H] and [Fe/Mg] for the fiducial model.

larger range of metallicities than thin disk stars. However, metal-poor abundance measurments require consideration of 3D-NLTE effects, which can be an ~0.2 dex effect (e.g. CITE). Finally, dwarf galaxies, damped Lyman-alpha systems, and extragalactic regions may represent different SFHs than the Milky Way. As AGB C production is sensitive to variations in the SFH, these environments may not exactly match our subgiant sample, limiting the usefulness of these abundance measurments in evaluating our model.

C lines are relatively faint, and surveys such as GALAH struggle against low detection rates, potentially biasing sample measurments. (e.g. gaia-eso AS WELL Franchini et al. 2020). In the gas phase, HII regions are our best window into C abundances. Unfortunantly, C lacks strong collisional excitation lines, and recombination lines fall in the ultraviolet without nearby reference H lines (Skillman et al. 2020). Recombination-line and collisional-excitation-line measurements furthermore disagree by a factor of ~2 (García-Rojas & Esteban 2007).

Fig. 10 shows the single-zone model and time-slices of the fiducial multi-zone model at present day and $t = 2\,\mathrm{Gyr}$. Here, we consider a single-zone model with parameters consistant with the Gaia-Encelidus sausage[5]. We chose the model to have mass loading $\eta = 20$, star formation efficiency $\tau_\star = 16\,\mathrm{Gyr}$, and a star formation history $\propto e^{-t/3\,\mathrm{Gyr}}$, evolved for 2 Gyr (Johnson et al. 2022). The single-zone model is better able to replicate the slope of the abundances in dwarf galaxies, HII-regions, and halo stars. The single-zone model does not produce an equilibrium track, unlike the multi-zone models. As the single-zone model also evolves slower, the late contribution of AGB stars causes the steeper slope at near-solar metallicities. By including an increase of C yields at low-metallicity, the single-zone model is also able to reproduce the increasing [C/O] abundances with decreasing metallicity past $[\mathrm{O/H}] < -1.5$. In any case, there is large scatter in the measurments, which both models fall within.

[5] See e.g. CITATION. Th Gaia-Encelidus sausage (GSE) is a kinematically and chemically distinct group of halo stars consistant with the merger of a dwarf galaxy early in the Milky Way's formation.

6 CONCLUSIONS

In this work, we investigated the role of C yields on the predictions of multi-zone GCE models. We began by adopting an equilibrium approximation to estimate the total C yields with metallicity from APOGEE subgiant [C/Mg]-[Mg/H] trends. We find that $y_\mathrm{C}/y_\mathrm{O} = 1/3 + 4(Z - Z_\odot)$ and $y_\mathrm{C}/y_\mathrm{Mg} = 2.7 + 32(Z - Z_\odot)$, where we assume $[\mathrm{Mg/O}] = 0$. We show that [C/Mg]-[Mg/H] is a diagnostic for total C yields with metallicity, but [C/Mg]-[Mg/Fe] provides information about delayed C production. From the [C/Mg]-[Mg/Fe] trends, we estimate that AGB stars with masses between about 1 and 3 $\mathrm{M}_\odot$contribute ~20% of total C abundances. In this model, the remaining ~80% of C comes from high-mass stars with a metallicity dependent yield of $y_\mathrm{C}^\mathrm{cc}/y_\mathrm{Mg} = 2.2 + 55(Z/Z_\odot)$, broadly consistant with rotating CCSNe models.

We additionally explore variations of the assumed SFH and outflow mass-loading factor η. We find that alternate SFHs can perturb [C/Mg]-[Mg/Fe]and [C/Mg]-[Mg/H] abundances slightly. Decreasing both outflows and yields by the same factor leaves the [C/Mg]-[Mg/H] and [C/Mg]-[Mg/Fe] trends unaffected, ingoring effect to the metallitict distribution of starrs. These constraints on the relative yields of C, O, and Mg are robust against variations in η.

Finally, we compare our model against gas-phase measurements and Milky Way halo stars. By including yields which are enhanced at low metallicities, CCSNe and AGB stars together are able to explain the general trends of C from metallicities of $[\mathrm{O/H}] = -3$ to 0.5.

Our C yield constraints provide a useful benchmark for stellar evolution models. C yields are sensitive to poorly understood processes, including mass-loss prescriptions, explodability, nuclear cross sections, convection, and stellar structure. Future spectroscopic surveys combined with Gaia kinematics (Gaia Collaboration et al. 2016) will continue to enhance our understanding of chemical evolution. Both the Sloan Digital Sky Survey V's Milky Way Mapper program (SDSS-V/MWM) (Kollmeier et al. 2017) and the Dark Energy Spectroscopic Instrument (DESI) Milky Way survey (DESI Collaboration et al. 2016; Cooper et al. 2022) will each measure spectra of upwards 6,000,000 Milky Way stars. These larger samples will enable similar

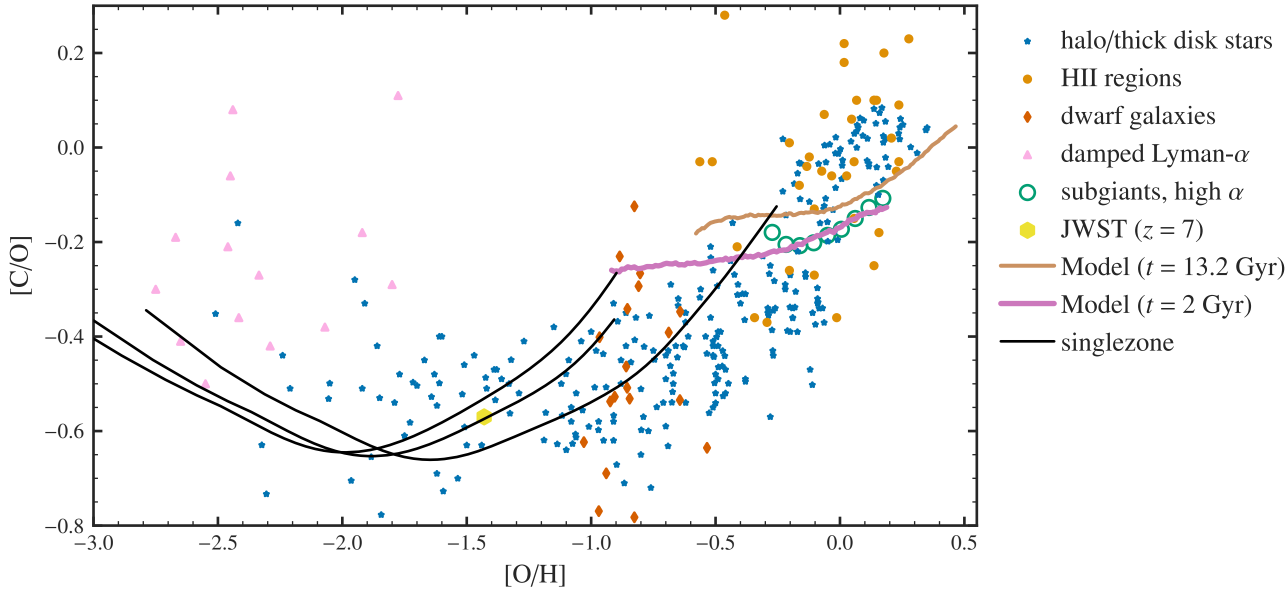

Figure 10. Gas-phase C abundances. We plot our model at $t = 2$ Gyr and present day as thick solid lines. Black lines are single-zone models. Points represent measurements in HII regions (pink circles; Skillman et al. 2020; Esteban et al. 2002, 2009, 2014, 2019) damped Lyman-alpha (DLA) systems (blue triangles; Ellison et al. 2010; Srianand et al. 2010; Dutta et al. 2014; Dessauges-Zavadsky et al. 2003; Pettini et al. 2008; Morrison et al. 2016; Cooke et al. 2017), dwarf galaxies (red diamonds; Berg et al. 2019), Milky Way halo and thick disk stars (green stars; Amarsi et al. 2019; Nissen et al. 2014; Fabbian et al. 2009), and Milky Way high-α stars (yellow points; Robert et al. 2023, in prep.).

work to tighten constraints on stellar models and our understanding of galaxy structure and evolution.

ACKNOWLEDGEMENTS

Here you can thank helpful colleagues, acknowledge funding agencies, telescopes and facilities used etc. Try to keep it short.

Software that has contributed to this work included VICE (Johnson & Weinberg 2020; Johnson et al. 2021), MATPLOTLIB (Hunter 2007), SCIPY (Virtanen et al. 2020), IPYTHON (Pérez & Granger 2007), PANDAS (pandas development team 2020), NUMPY (Harris et al. 2020), ASTROPY (Astropy Collaboration et al. 2013, 2018, 2022), and SEABORN (Waskom 2021) . Additionally, we thank Ohio Supercomputer Center (1987) for the use of its facilities for the simulations.

DATA AVAILABILITY

The inclusion of a Data Availability Statement is a requirement for articles published in MNRAS. Data Availability Statements provide a standardised format for readers to understand the availability of data underlying the research results described in the article. The statement may refer to original data generated in the course of the study or to third-party data analysed in the article. The statement should describe and provide means of access, where possible, by linking to the data or providing the required accession numbers for the relevant databases or DOIs.

REFERENCES

Adelberger E. G., et al., 2011, Reviews of Modern Physics, 83, 195
Amarsi A. M., Nissen P. E., Skúladóttir Á., 2019, A&A, 630, A104
Asplund M., Grevesse N., Sauval A. J., Scott P., 2009, ARA&A, 47, 481
Astropy Collaboration et al., 2013, A&A, 558, A33
Astropy Collaboration et al., 2018, AJ, 156, 123
Astropy Collaboration et al., 2022, ApJ, 935, 167
Bensby T., Feltzing S., 2006, MNRAS, 367, 1181
Berg D. A., Erb D. K., Henry R. B. C., Skillman E. D., McQuinn K. B. W., 2019, ApJ, 874, 93
Bird J. C., Kazantzidis S., Weinberg D. H., 2012, MNRAS, 420, 913
Bird J. C., Kazantzidis S., Weinberg D. H., Guedes J., Callegari S., Mayer L., Madau P., 2013, ApJ, 773, 43
Bird J. C., Loebman S. R., Weinberg D. H., Brooks A. M., Quinn T. R., Christensen C. R., 2021, MNRAS, 503, 1815
Bland-Hawthorn J., Gerhard O., 2016, ARA&A, 54, 529
Brooks A. M., Zolotov A., 2014, ApJ, 786, 87
Chiappini C., Romano D., Matteucci F., 2003, MNRAS, 339, 63
Christensen C., Quinn T., Governato F., Stilp A., Shen S., Wadsley J., 2012, MNRAS, 425, 3058
Cooke R. J., Pettini M., Steidel C. C., 2017, MNRAS, 467, 802
Cooper A. P., et al., 2022, arXiv e-prints, p. arXiv:2208.08514
Cristallo S., et al., 2011, ApJS, 197, 17
Cristallo S., Straniero O., Piersanti L., Gobrecht D., 2015, ApJS, 219, 40
DESI Collaboration et al., 2016, arXiv e-prints, p. arXiv:1611.00036
Dalcanton J. J., 2007, ApJ, 658, 941
Dearborn D. S. P., Tinsley B. M., Schramm D. N., 1978, ApJ, 223, 557
Dessauges-Zavadsky M., Péroux C., Kim T. S., D'Odorico S., McMahon R. G., 2003, MNRAS, 345, 447
Dutta R., Srianand R., Rahmani H., Petitjean P., Noterdaeme P., Ledoux C., 2014, MNRAS, 440, 307
Ellison S. L., Prochaska J. X., Hennawi J., Lopez S., Usher C., Wolfe A. M., Russell D. M., Benn C. R., 2010, MNRAS, 406, 1435
Esteban C., Peimbert M., Torres-Peimbert S., Rodríguez M., 2002, ApJ, 581, 241
Esteban C., Bresolin F., Peimbert M., García-Rojas J., Peimbert A., Mesa-Delgado A., 2009, ApJ, 700, 654
Esteban C., García-Rojas J., Carigi L., Peimbert M., Bresolin F., López-Sánchez A. R., Mesa-Delgado A., 2014, MNRAS, 443, 624

Esteban C., García-Rojas J., Arellano-Córdova K. Z., Méndez-Delgado J. E., 2019, arXiv e-prints, p. arXiv:1905.10129
Fabbian D., Nissen P. E., Asplund M., Pettini M., Akerman C., 2009, A&A, 500, 1143
Farmer R., Laplace E., de Mink S. E., Justham S., 2021, ApJ, 923, 214
Finlator K., Davé R., 2008, MNRAS, 385, 2181
Franchini M., et al., 2020, ApJ, 888, 55
Frankel N., Rix H.-W., Ting Y.-S., Ness M., Hogg D. W., 2018, ApJ, 865, 96
Frankel N., Sanders J., Ting Y.-S., Rix H.-W., 2020, ApJ, 896, 15
Frinchaboy P. M., et al., 2013, ApJ, 777, L1
Gaia Collaboration et al., 2016, A&A, 595, A1
García Pérez A. E., et al., 2016, AJ, 151, 144
García-Rojas J., Esteban C., 2007, ApJ, 670, 457
Gilroy K. K., 1989, ApJ, 347, 835
Griffith E. J., Sukhbold T., Weinberg D. H., Johnson J. A., Johnson J. W., Vincenzo F., 2021, ApJ, 921, 73
Harris C. R., et al., 2020, Nature, 585, 357
Hayden M. R., et al., 2014, AJ, 147, 116
Henry R. B. C., Edmunds M. G., Köppen J., 2000, ApJ, 541, 660
Hunter J. D., 2007, Computing in Science & Engineering, 9, 90
Iben Icko J., 1967, ARA&A, 5, 571
Isern J., 2019, ApJ, 878, L11
Johnson J. A., 2019, Science, 363, 474
Johnson J. W., Weinberg D. H., 2020, MNRAS, 498, 1364
Johnson J. W., et al., 2021, MNRAS, 508, 4484
Johnson J. W., et al., 2022, arXiv e-prints, p. arXiv:2210.01816
Johnson J. W., Weinberg D. H., Vincenzo F., Bird J. C., Griffith E. J., 2023, MNRAS, 520, 782
Karakas A. I., 2010, MNRAS, 403, 1413
Karakas A. I., Lattanzio J. C., 2014, Publ. Astron. Soc. Australia, 31, e030
Karakas A. I., Lugaro M., 2016, ApJ, 825, 26
Karakas A. I., Lugaro M., Carlos M., Cseh B., Kamath D., García-Hernández D. A., 2018, MNRAS, 477, 421
Kennicutt Robert C. J., 1998, ARA&A, 36, 189
Kobayashi C., Karakas A. I., Lugaro M., 2020, ApJ, 900, 179
Kollmeier J. A., et al., 2017, arXiv e-prints, p. arXiv:1711.03234
Korn A. J., Grundahl F., Richard O., Mashonkina L., Barklem P. S., Collet R., Gustafsson B., Piskunov N., 2007, ApJ, 671, 402
Kroupa P., 2001, MNRAS, 322, 231
Larson R. B., 1972, Nature Physical Science, 236, 7
Larson R. B., 1974, MNRAS, 166, 585
Licquia T. C., Newman J. A., 2015, ApJ, 806, 96
Lilly S. J., Carollo C. M., Pipino A., Renzini A., Peng Y., 2013, ApJ, 772, 119
Limongi M., Chieffi A., 2018, ApJS, 237, 13
Lind K., Korn A. J., Barklem P. S., Grundahl F., 2008, A&A, 490, 777
Loebman S. R., Ivezić Ž., Quinn T. R., Governato F., Brooks A. M., Christensen C. R., Jurić M., 2012, ApJ, 758, L23
Majewski S. R., et al., 2017, AJ, 154, 94
Maoz D., Mannucci F., Brandt T. D., 2012, MNRAS, 426, 3282
Matteucci F., 2021, A&ARv, 29, 5
Minchev I., Chiappini C., Martig M., 2013, A&A, 558, A9
Minchev I., Chiappini C., Martig M., 2014, A&A, 572, A92
Mor R., Robin A. C., Figueras F., Roca-Fàbrega S., Luri X., 2019, A&A, 624, L1
Morrison S., Kulkarni V. P., Som D., DeMarcy B., Quiret S., Péroux C., 2016, ApJ, 830, 158
Nissen P. E., Chen Y. Q., Carigi L., Schuster W. J., Zhao G., 2014, A&A, 568, A25
Nomoto K., Kobayashi C., Tominaga N., 2013, ARA&A, 51, 457
Ohio Supercomputer Center 1987, Ohio Supercomputer Center, `http://osc.edu/ark:/19495/f5s1ph73`
Pagel B. E. J., 2009, Nucleosynthesis and Chemical Evolution of Galaxies, 2 edn. Cambridge University Press, doi:10.1017/CBO9780511812170
Peeples M. S., Shankar F., 2011, MNRAS, 417, 2962
Pérez F., Granger B. E., 2007, Computing in Science and Engineering, 9, 21
Pettini M., Zych B. J., Steidel C. C., Chaffee F. H., 2008, MNRAS, 385, 2011
Prantzos N., Abia C., Limongi M., Chieffi A., Cristallo S., 2018, MNRAS, 476, 3432
Romano D., 2022, A&ARv, 30, 7
Romano D., Karakas A. I., Tosi M., Matteucci F., 2010, A&A, 522, A32
Rybizki J., Just A., Rix H.-W., 2017, A&A, 605, A59
Sánchez S. F., 2020, ARA&A, 58, 99
Sellwood J. A., Binney J. J., 2002, MNRAS, 336, 785
Skillman E. D., Berg D. A., Pogge R. W., Moustakas J., Rogers N. S. J., Croxall K. V., 2020, ApJ, 894, 138
Souto D., et al., 2018, ApJ, 857, 14
Souto D., et al., 2019, ApJ, 874, 97
Spitoni E., Silva Aguirre V., Matteucci F., Calura F., Grisoni V., 2019, A&A, 623, A60
Spitoni E., Verma K., Silva Aguirre V., Calura F., 2020, A&A, 635, A58
Spitoni E., et al., 2021, A&A, 647, A73
Srianand R., Gupta N., Petitjean P., Noterdaeme P., Ledoux C., 2010, MNRAS, 405, 1888
Sukhbold T., Ertl T., Woosley S. E., Brown J. M., Janka H. T., 2016, ApJ, 821, 38
Tacconi L. J., et al., 2018, ApJ, 853, 179
Tinsley B. M., 1979, ApJ, 229, 1046
Tinsley B. M., 1980, Fundamentals Cosmic Phys., 5, 287
Ventura P., Di Criscienzo M., Carini R., D'Antona F., 2013, MNRAS, 431, 3642
Ventura P., Dell'Agli F., Schneider R., Di Criscienzo M., Rossi C., La Franca F., Gallerani S., Valiante R., 2014, MNRAS, 439, 977
Ventura P., Karakas A., Dell'Agli F., García-Hernández D. A., Guzman-Ramirez L., 2018, MNRAS, 475, 2282
Ventura P., Dell'Agli F., Lugaro M., Romano D., Tailo M., Yagüe A., 2020, A&A, 641, A103
Vincenzo F., et al., 2021, arXiv e-prints, p. arXiv:2106.03912
Virtanen P., et al., 2020, Nature Methods, 17, 261
Waskom M. L., 2021, Journal of Open Source Software, 6, 3021
Weinberg D. H., Andrews B. H., Freudenburg J., 2017, ApJ, 837, 183
Weinberg D. H., et al., 2019, ApJ, 874, 102
Weinberg D. H., et al., 2022, ApJS, 260, 32
Woosley S. E., Weaver T. A., 1995, ApJS, 101, 181
Zolotov A., et al., 2012, ApJ, 761, 71
pandas development team T., 2020, pandas-dev/pandas: Pandas, doi:10.5281/zenodo.3509134, `https://doi.org/10.5281/zenodo.3509134`

This paper has been typeset from a TEX/LATEX file prepared by the author.